36th AIAA Fluid Dynamics Conference, June 5-8, 2006, San Francisco, California

Computational Analysis of Dual Radius Circulation Control Airfoils

E. M. Lee-Rausch * V. N. Vatsa † C. L. Rumsey ‡

I. Abstract

The goal of the work is to use multiple codes and multiple configurations to provide an assessment of the capability of RANS solvers to predict circulation control dual radius airfoil performance and also to identify key issues associated with the computational predictions of these configurations that can result in discrepancies in the predicted solutions. Solutions were obtained for the Georgia Tech Research Institute (GTRI) dual radius circulation control airfoil and the General Aviation Circulation Control (GACC) dual radius airfoil. For the GTRI-DR airfoil, two-dimensional structured and unstructured grid computations predicted the experimental trend in sectional lift variation with blowing coefficient very well. Good code–to–code comparisons between the chordwise surface pressure coefficients and the solution streamtraces also indicated that the detailed flow characteristics were matched between the computations. For the GACC-DR airfoil, two-dimensional structured and unstructured grid computations predicted the sectional lift and chordwise pressure distributions accurately at the no blowing condition. However at a moderate blowing coefficient, although the code–to–code variation was small, the differences between the computations and experiment were significant. Computations were made to investigate the sensitivity of the sectional lift and pressure distributions to some of the experimental and computational parameters, but none of these could entirely account for the differences in the experimental and computational results. Thus, CFD may indeed be adequate as a prediction tool for dual radius CC flows, but limited and difficult to obtain two-dimensional experimental data prevents a confident assessment at this time.

II. Introduction

Circulation control (CC) technology has great potential for use in the next generation of aeronautical vehicles. There has also been interest in CC technologies for naval applications. CC not only has the capability to delay or eliminate separation through boundary layer control, but it also can augment an airfoil's circulation considerably, thus enhancing maximum lift. In order to evaluate and design individual CC technologies as well as integrate these technologies onto a vehicle, accurate and robust analysis tools are needed. Recent studies have focused on assessing and validating the capabilities of computational fluid dynamics (CFD) to predict the performance of different flow control technologies including synthetic jets[1] and CC airfoils.[2] The CFD codes were validated through code–to–code comparisons as well as through comparison with experimental data. Although the circular trailing edge CC airfoil has been the focus of the CC Workshop and other CFD studies,[3–6] the dual radius CC airfoil developed by Englar[7] is also of interest for aeronautical applications because it has the potential to alleviate the high cruise drag associated with the circular trailing edge airfoil. The dual radius CC airfoil concept was tested by Englar[7] at Georgia Tech Research Institute (GTRI) and more recently by Jones at NASA LaRC as a modification to a General Aviation Circulation Control (GACC) airfoil.[10]

Previous computational studies[2,6] indicated that current CFD methods did not predict the circular Coanda flows robustly or accurately. The separation location on the Coanda surface was very sensitive to computational parameters including turbulence models and tended to overpredict the performance (lift) of the airfoil in comparison with the

*Senior Member AIAA, Research Engineer NASA Langley Research Center(LaRC), Hampton, Virginia.
†Senior Member, AIAA, Senior Research Scientist NASA LaRC.
‡Associate Fellow AIAA, Senior Research Scientist NASA LaRC.

experiment due to a delay in jet separation. In some cases, the CFD solutions predicted a physically unrealistic wrapping of the streamlines all the way around the airfoil. There were also questions regarding the precise conditions in the experiment including blowing rate and three-dimensional effects.

With the dual-radius CC configuration, the sharp trailing edge effectively fixes separation and avoids the potential for jet wraparound. Numerical simulations of the dual-radius CC airfoils has been limited. Computational analysis of the GTRI dual radius configuration by Lui et al. with a two-dimensional structured–grid code predicted the performance characteristics of the airfoil well.[8] In Ref. 8, Lui et al. studied the effects of leading edge blowing, free-stream velocity, jet-slot height and blowing frequency on the performance of two-dimensional steady and pulsed CC jets. The computations in Ref. 8 accurately predicted the sectional lift coefficient variation with blowing coefficients at the lower geometric angles of attack. However, at the higher angles of attack the computations stalled early. The current work will also focus on the computational analysis of the dual radius CC airfoil tested by Englar[7] as well as the GACC dual radius airfoil tested by Jones.[10] Code–to–code comparisons between three Reynolds-Averaged Navier-Stokes (RANS) codes are made as well as comparisons with experimental data. The three codes used for the analysis include two structured grid codes, TLNS3D and CFL3D, and one unstructured grid code, FUN3D. The primary goal of the work is to use multiple codes and multiple configurations to provide an assessment of the capability of RANS solvers to robustly predict CC dual radius airfoil performance. A second goal is to identify key issues associated with CFD analysis of these types of flow control configurations that can result in discrepancies in the predicted solutions.

III. Test Configurations and Data

A. GTRI Dual Radius Airfoil

The GTRI CC dual radius airfoil is one of several CC airfoil configurations tested in the GTRI Model Test Facility (MTF) 30 inch by 43 inch subsonic research tunnel.[7] The configuration to be analyzed in this study (GTRI-DR) is a 16% thick supercritical airfoil that has a 7.85 inch chord, a 30 inch span and a 30° flap angle. Figure 1(a) shows the airfoil profile of the baseline supercritical airfoil which has an 8.0 inch chord with the dual radius flap profile at the 30° flap angle. Note that the baseline airfoil chord length of 8.0 inches is used as the length non-dimensionalize parameter ($C = 8.0$). The dual-radius flap to airfoil chord radius is $c_f/C = 0.0955$ and the dual radius flap angle is $\delta_f = 30^\circ$ from the waterline. The jet slot height to chord ratio $h/C = 0.00191$. The experiment was performed with free transition. Experimental test data include force measurements, slot mass flow, jet plenum total pressure/temperature and blowing coefficient, C_μ. Note that the experimental blowing coefficient is defined as

$$\mathbf{C}_\mu = \frac{\dot{m}V_j}{\frac{1}{2}\rho_\infty U_\infty^2 A} \tag{1}$$

where ρ_∞ and U_∞ are the freestream density and velocity, respectively, and A is the airfoil chord length multiplied by the span. The experimental mass flow rate values ($\dot{m}$) were measured using a calibrated meter in the air supply line and the jet velocity, V_j, was calculated as an isentropic expansion from the duct pressure to the freestream static pressure. The experimental set-up employed blowing treatment along the wind tunnel walls for alleviating the model/wall juncture vortical flows. Estimates of angle of attack corrections for wall interference and streamline curvature have been provided.

B. GACC Dual Radius Airfoil

The GACC model was designed around the mass flow actuation system and sized to fit into the LaRC BART wind tunnel.[9] The model was originally tested with a circular trailing edge configuration. More recently the model was retested in the BART tunnel with a dual-radius trailing edge.[10] The GACC dual-radius airfoil (GACC-DR) is a 17% thick supercritical airfoil that has a 10.014 inch chord and a 28 inch span. The experimental results were obtained over a Mach number range of 0.082 to 0.1 corresponding to dynamic pressure of 10 psf and 15 psf, respectively. The dual-radius flap to airfoil chord radius is $c_f/C = 0.088$ and the dual radius flap angle is $\delta_f = 57^\circ$ from the waterline (See Fig. 1(b)). The jet slot height to chord ratio $h/C = 0.00099$. (The jet slot height noted in Fig. 1(b) is for the circular trailing edge configuration.) The experiment was performed with free transition. Experimental test data include force measurements from a five–component strain gage balance, centerline steady surface pressure measurements, centerline PIV measurement for steady and pulsed blowing conditions, slot mass flow, jet plenum total pressure/temperature and blowing coefficient, C_μ. Note that the experimental blowing coefficient is defined as in Eq. 1. The experiment employed no suction or blowing treatment along the wind tunnel walls for alleviating the model/wall juncture vortical

flows. Note that wall interference corrections have not been applied to any of the GACC-DR experimental data shown in this paper.

IV. Flow Solvers

A. FUN3D Flow Solver

FUN3D[11–13] is a finite-volume RANS solver in which the flow variables are stored at the vertices of the mesh. FUN3D solves the equations on mixed element grids, including tetrahedra, pyramids, prisms, and hexahedra and has now has a two-dimensional path for triangular grids. It employs an implicit upwind algorithm in which the inviscid fluxes are obtained with a flux-difference-splitting scheme of Roe and the viscous terms are evaluated with a finite-volume formulation, which is equivalent to a Galerkin type of approximation for these terms. This formulation results in a discretization of the full Navier-Stokes terms without any thin-layer approximations for the viscous terms. At interfaces delimiting neighboring control volumes, the inviscid fluxes are computed using as approximate Riemann solver based on the values on either side of the interface. For second-order accuracy, interface values are obtained by extrapolation of the control volume centroidal values, based on gradients computed at the mesh vertices using an unweighted least-squares technique. The solution at each time-step is updated with a backwards Euler time-differencing scheme. At each time step, the linear system of equations is approximately solved with either a point implicit procedure or an implicit line relaxation scheme.[14] Local time-step scaling is employed to accelerate convergence to steady-state. FUN3D is able to solve the RANS flow equations, either tightly or loosely coupled to the Spalart-Allmaras[15] (S-A) one-equation turbulence model. In this investigation all computations are loosely coupled and assume fully turbulent flow.

B. TLNS3D Flow Solver

The TLNS3D code is a multiblock structured grid solver that utilizes the generalized thin-layer Navier-Stokes equations as the governing equations.[16] The spatial terms are discretized using the cell-centered finite volume scheme with artificial dissipation added for stability. Time is discretized in a fully implicit sense by using either a multistep BDF or multistage Runge-Kutta scheme. The resultant nonlinear algebraic equations are solved iteratively in pseudo-time with a multigrid acceleration used to speed up the convergence. The Spalart-Allmaras turbulence model is also used in this investigation and all computations assume fully turbulent flow.

C. CFL3D Flow Solver

CFL3D is a structured-grid upwind multi-zone CFD code that solves the generalized thin-layer Navier-Stokes equations.[17] It can use point-matched, patched, or overset grids and employs local time-step scaling, grid sequencing and multigrid to accelerate convergence to steady stage. A time-accurate mode is available, and the code can employ low-Mach number preconditioning for accuracy in computing low-speed steady-state flows. CFL3D is a cell-centered finite-volume method. It uses third-order upwind-biased spatial differencing on the convective and pressure terms, and second-order differencing on the viscous terms; it is globally second-order accurate. Roe's flux difference-splitting (FDS) method[18] is used to obtain fluxes at the cell faces. The solution is advanced in time with an implicit approximate factorization method. A wide variety of eddy-viscosity turbulence models are available in the code, including nonlinear models. Both the Spalart-Allmaras turbulence model and the Menter SST model[19] were used in this study. All computations are assumed fully turbulent.

V. Computational Results

A. Dual Radius Airfoil Grids and Boundary Conditions

The 2D multi-block structured grids for the GTRI-DR and GACC-DR were generated with the Gridgen commercial software package. Partial views of the GTRI-DR airfoil structured grid are shown in Fig. 2(b). The grid has 39 blocks and a total of 130,304 cells. There are 529 points on the airfoil exterior no-slip surface. The outer boundary is located 30 chord lengths away from the airfoil. In the wall normal direction, the grid spacing is set such that an average normalized coordinate y^+ is less than one for the first grid cell at the wall for the main airfoil. The values of y^+ on the dual-radius flap are less than one for the no–blowing case, but increases above one at the higher blowing rates. The effect of the higher y^+ values on the solution will be discussed later in the paper. A close–up view of the structured

grid jet slot region of the GTRI-DR airfoil in Fig. 2 shows that the jet plenum chamber is modeled far inside of the slot. Total temperature and pressure boundary conditions are applied at the upstream wall of the chamber to match the measured experimental conditions. In the computation, given total pressure ratio, total temperature, and flow angle, the pressure is extrapolated from the interior of the domain, and the remaining variables are determined from the extrapolated pressure and the input data, using isentropic relations. No-slip boundary conditions are applied to all other airfoil surfaces except the blunt trailing edge at the jet slot lip and on the flap, where slip boundary conditions were used.

The 2D unstructured triangular grid for the GTRI-DR was generated with the AFLR2 advancing-front grid generation code. Partial views of the GTRI-DR airfoil unstructured grid are shown in Fig. 3. The grid has 110,164 nodes with 935 nodes on the no-slip airfoil surface. The outer boundary is located 20 chord lengths away from the airfoil. In the wall normal direction, the grid spacing is set such that on the main airfoil an average normalized coordinate y^+ is less than one for the first node off the wall. As with the structured grid results, the values of y^+ on the dual-radius flap increase above one at the higher blowing rates. A close up view of the jet slot region in the unstructured grid is also shown in Fig. 3(b). Static temperature and normal mass flow boundary conditions are applied at the upstream wall of the chamber to match the experimental total pressure ratio, total temperature conditions in the inlet of the plenum. No-slip boundary conditions are applied to all other airfoil surfaces.

The grids for the GACC-DR airfoil were developed in a similar manner. The structured grid has 34 blocks and a total of 363,150 cells. There are 550 points on the airfoil exterior no-slip surface. A close up view of the structured grid jet slot region of the GACC-DR airfoil in Fig. 4(a) shows that the jet plenum chamber is modeled far inside of the slot. The GACC-DR unstructured grid has 142,642 nodes with 2,050 nodes on the no-slip airfoil surface. A close up view of the jet slot region in the unstructured grid, which extends farther upstream than the structured grid, is also shown in Fig. 4(b). Similar to the GTRI-DR configurations, static temperature and normal mass flow boundary conditions are applied at the upstream wall of the chamber to match the experimental total pressure ratio, total temperature conditions in the inlet of the plenum.

B. GTRI Dual Radius Airfoil

The GTRI-DR airfoil was analyzed over a range of blowing coefficients corresponding to the experimental 0° geometric angle of attack. The freestream conditions for this configuration correspond to a Mach number of 0.0842 and a chord Reynolds number of 0.37 million. In this study, all calculations are performed with the SA turbulence model. The angle of attack corrections range from -0.005° at $C_\mu = 0$ to -0.056° at $C_\mu = 0.374$. Note that for all computations in this study, the computational blowing coefficient is computed using the same definitions as the experimentally derived value (See Eq. 1). The variation of experimental and computational sectional lift coefficient, C_l, with blowing coefficient for the GTRI-DR is shown in Fig. 5(a). Computations were performed with FUN3D and CFL3D at the jet plenum conditions corresponding to the experimental blowing coefficients $C_\mu = 0, 0.11, 0.22, 0.32$ and 0.37 (CFL3D only). As indicated in Fig. 5(a), both the FUN3D and CFL3D computations predict the experimental trend in lift coefficient variation with C_μ very well. Note that when the total pressure and temperature conditions are matched between the experiment and computation, the computational jet mass flow rate for that condition does not match up with the experimentally measured mass flow rate, which results in an offset in C_μ for the computational and experimental data points in Fig. 5(a). The reason for this discrepancy is not known. Figure 5(b) also shows C_l vs. C_μ for the GACC-DR airfoil to make direct comparison between the two airfoils easier. These GACC-DR results will be discussed in the next section.

The good code-to-code comparison of sectional lift coefficient for the GTRI-DR indicates that both codes are predicting similar performance characteristics for the airfoil. Code-to-code comparisons of chordwise pressure coefficients at multiple blowing coefficients in Figs. 6, 7, and 8 indicate how well the detailed flow characteristics are matched between the computations. At the $C_\mu = 0$ condition shown in Fig. 6, the FUN3D and CFL3D surface pressure results compare very well over the entire airfoil. Similarly at $C_\mu = 0.11$ shown in Fig. 7, the computational surface pressure results compare very well over the entire airfoil. At $C_\mu = 0.32$ condition shown in Fig. 8, there are slight differences in the recompression area on the flap upper surface. The FUN3D results show a kink in the surface distribution on the upper flap at the interface of the dual radius surfaces that is not present in the CFL3D solutions.

As the C_μ values increase, the maximum y^+ values on the upper flap surface also increased in the jet region over the flap to almost four in the CFL3D solution and almost seven in the FUN3D solution. The effect of the larger y^+ values was studied by generating a new unstructured grid with the same surface point distributions but with the wall spacing reduced by a factor of four. FUN3D results for the $C_\mu = 0.32$ case on the new mesh with refinement in the normal wall spacing is shown in Fig. 9 in comparison with the CFL3D results from Fig. 8. The maximum y^+ value on the upper flap for the FUN3D solution is reduced to just below two. The sectional lift coefficient increases slightly

from $C_l = 3.79$ to 3.84 with the normal grid spacing refinement. The kink in the pressure distribution is reduced and the code-to-code comparison of surface pressure is improved on the flap. As noted in Fig. 9 the code-to-code comparison of sectional lift coefficient is also slightly improved.

Code-to-code comparisons of streamtraces at multiple blowing coefficients in Fig. 10(a), (b), and (c) also indicate how well the detailed flow characteristics are matched between the computations. In Fig. 10(a), both codes predict the separation on the flap at $C_\mu = 0$. At $C_\mu = 0.11$ in Fig. 10(b), both codes predict similar turning of the leading and trailing edge stagnation streamlines with a small area of separation in the lower flap cove. At the higher blowing coefficient $C_\mu = 0.32$ in Fig. 10(c), both codes predict the increase in the turning of the leading and trailing edge stagnation streamlines which produces the increased sectional lift coefficient.

C. GACC Dual Radius Airfoil

The GACC-DR airfoil was analyzed at the 10 psf experimental condition where a majority of the PIV and hot wire data were taken. This dynamic pressure corresponds to a freesteam Mach number of 0.0824 and a chord Reynolds number of 0.47 million. The majority of the data were taken at a 0° geometric angle of attack. Note that for all computations in this study, the computational blowing coefficient is computed using the same definitions as the experimentally derived value (See Eq. 1). All calculations are performed with the SA model unless otherwise noted.

Although no angle of attack corrections were applied to the experimental data, past experience with CC airfoil data led the authors to initially investigate the effects of induced angle of attack from the wind tunnel wall/model juncture vortices. The following formula based on geometric angle of attack, α_{geo}, and the experimentally measured sectional lift coefficient, C_{lexp}, estimates an effective angle of attack, $\alpha_{eff} = \alpha_{geo} - 1.5C_{lexp}$. Figure 11 shows a comparison of experimental chordwise pressure coefficients with the FUN3D calculations at the geometric and estimated effective angles of attack for the no blowing condition, $C_\mu = 0$. Figure 12 shows a similar comparison for $C_\mu = 0.09$. The corresponding experimental and computational lift coefficients are also included in the plots. The computational results indicate that the angle of attack correction provides a rational level of adjustment to achieve agreement with the measured upper surface pressure peaks and sectional lift coefficient.

The variation of experimental and computational sectional lift coefficient, C_l, with blowing coefficient for the GACC-DR is shown in Fig. 5(b) with the computations being performed at the estimated effective angles of attack. Even with the estimated angle-of-attack corrections, the computed sectional lift coefficient at $C_\mu = 0.09$ are significantly higher (by about 30%) than the experimental value. Figure 12 also indicates that with jet blowing the CFD is predicting too high a level of circulation, yielding pressure levels that are somewhat low over the entire upper airfoil surface.

Computations were made to investigate the sensitivity of the sectional lift coefficient and pressure distributions to some of the experimental parameters. FUN3D computations to assess the sensitivity of the lift coefficient to mass blowing rate indicate that a drop of 10% in mass flow will result in a 10% drop in lift coefficient. FUN3D computations investigating the effects of jet slot expansion under pressure indicate that a 0.003 inch expansion of the slot resulting in a 30% increase in slot width, which will reduce the lift coefficient to 3.76 (an 8.25% descrease from the baseline configuration). Computations modeling the upper and lower wind tunnel walls indicated a negligible effect on the airfoil lift coefficient and pressure distributions.

Computations were also made to investigate the sensitivity of the sectional lift coefficient and pressure distributions to some of the numerical/computational parameters. Figure 13 shows a comparison of the chordwise pressure distributions between the three CFD codes with no blowing for the experimental $\alpha_{geom} = 0^\circ$ angle of attack. The experimental data is included for comparison. There is little code-to-code variation for this condition except on the upper surface of the dual-radius flap. All codes tend to prematurely separate on the lower surface of the airfoil. This may be due to a difference between the location of transition in the experiment and the delay in the development of turbulent eddy viscosity that that occurs for "fully turbulent" low Reynolds number computations. Figure 14 compares CFD results from the three codes for a blowing coefficient of $C_\mu = 0.09$ and a corrected angle of attack of -4.62°. Like the no-blowing case, the 3 codes predict very consistent, similar results compared to each other. Figure 15 compares results using two different turbulence models for the same case. Although SST predicts a somewhat a lower lift coefficient than SA, the overall circulation is still significantly high compared to experiment. As with the GTRI-DR when the C_μ values increase, the maximum y^+ values on the upper flap surface also increase in the jet region over the flap. The effect of the larger y^+ values was studied on the GACC-DR by generating a new unstructured grid with the same surface point distributions but with the wall spacing reduced by a factor of six. For the new mesh with refinement in the normal wall spacing, the maximum y^+ value on the upper flap for the FUN3D solution at $C_\mu = 0.09$ is reduced to just below one. The sectional lift coefficient did not change from $C_l = 4.00$ with the normal grid spacing refinement, and there were no significant changes in the chordwise pressure coefficient.

It is not clear at this time what the root cause of the discrepancy between CFD and the GACC experimental data is. Although some of the experimental and numerical/computational parameters investigated lowered the lift coefficient, no single effect accounted for the total difference in the computational and experimental lift coefficient. Unfortunately, there are no experimental velocity profiles available in the jet exit region to serve as a check on how well the CFD jet boundary conditions are matching experiment. However, comparisons can be made of velocity profiles in the jet just below the trailing edge, as shown in Fig. 16. The CFD solutions predict a core jet velocity nearly twice as high as experiment. Thus, either the jet exit conditions are very different, or else the computed jet is not diffusing as quickly as in the experiment. If present, this latter effect could be caused by a deficiency in the turbulence modeling. However, it seems unlikely that the primary cause of the large discrepancy here is turbulence modeling, because the SA model did an excellent job predicting results for the GTRI airfoil.

VI. Summary

The goal of the work is to use multiple codes and multiple configurations to provide an assessment of the capability of RANS solvers to predict CC dual radius airfoil performance and also to identify key issues associated with the CFD predictions of these configurations that can result in discrepancies in the predicted solutions. The GTRI-DR airfoil was analyzed over a range of blowing coefficients corresponding to the experimental 0° geometric angle of attack. Two-dimensional structured and unstructured grid computations predicted the experimental trend in sectional lift coefficient variation with C_μ very well. Good code–to–code comparisons between the chordwise surface pressure coefficients and the solution streamtraces also indicated that the detailed flow characteristics were matched between the computations. There was no experimental surface pressure coefficients or off–surface flow measurements available for comparison with the computations. Although the wall normal grid spacing was sufficiently small for the no blowing cases, as the blowing coefficient was increased, the values of y^+ on the dual-radius flap increased above one. A refinement of the unstructured grid normal wall spacing indicated that larger y^+ values on the upper dual–radius flap surface did not have a significant effect on the final solution in terms of surface pressures or integrated lift coefficient.

For the GACC-DR airfoil, code–to–code comparisons between three RANS codes were made as well as comparisons with experimental data. Two-dimensional steady blowing and no blowing computations were performed, and the lift coefficient and chordwise pressure distributions were compared with GACC dual radius experimental data. The effects of angle of attack corrections were quantified as well as the sensitivity to turbulence model. The computational and experimental sectional lift coefficient and chordwise pressure distributions compared very well at $C_\mu = 0$. However at $C_\mu = 0.09$, although the code–to–code variation was small, the differences between the computations and experiment were significant. The comparisons of lift coefficient and chordwise pressure distribution between the experiment and the computations indicate that the circulation developed around the airfoil in the computation is much higher than that of the experiment. Comparisons were made of velocity profiles in the jet just below the trailing edge that indicated that the CFD solutions predicted a core jet velocity nearly twice as high as that in the experiment. Thus, either the jet exit conditions are very different, or else the computed jet is not diffusing as quickly as in the experiment

For the GTRI-DR airfoil, the RANS codes accurately predicted the effect of the jet blowing on the performance characteristics of the airfoil. However, for the GACC-DR airfoil, the RANS codes over-predicted the jet blowing effect. The cause for the discrepancies in the GACC-DR predictions is unknown. Computations were made to investigate the sensitivity of the sectional lift coefficient and pressure distributions to some of the experimental and computational parameters, but none of these could entirely account for the differences in the experimental and computational results. It is difficult to ensure that the computation is modeling the same jet exit conditions as the experiment without measurements of the velocity profile at the jet exit. Also truly two-dimensional experiments are extremely difficult to perform for high-lift flows, particularly because of the effects of strong wall-juncture vortical structures that influence the entire flowfield circulation. In the GTRI-DR experiment, side–wall blowing was used to alleviate this influence whereas in the GACC-DR experiment no side–wall control was employed. Thus, CFD may indeed be adequate as a prediction tool for dual radius CC flows, but limited and difficult to obtain two-dimensional experimental data prevents a confident assessment at this time.

VII. Acknowledgments

The authors would like to thank Dr. Gregory S. Jones of NASA Langley Research Center for providing the GACC dual-radius experimental data and Mr. Robert J. Englar of the Georgia Tech Research Institute for providing the GTRI dual-radius airfoil definition and experimental data. The authors would also like to thank Mr. Scott G. Anders of the NASA Langley Research Center for his many helpful discussion regarding the testing and analysis of circulation

control airfoils.

References

[1]Rumsey, C. L., Gatski, T. B., Sellers III, W. L., Vatsa, V. N., and Viken, S. A., "Summary of the 2004 CFD Validation Workshop on Synthetic Jets and Turbulent Separation Control," AIAA Paper 2004–2217, 2004.

[2]Jones, G. S. and Joslin, R. D. e., *Proceedings of the Circulation Control Workshop March 2004*, NASA CP-2005-213509, 2005.

[3]Slomski, J. F., Gorski, J. J., Miller, R. W., and Marino, T. A., "Numerical Simulation of Circulation Control Airfoils as Affected by Different Turbulence Models," AIAA Paper 2002–0851, 2002.

[4]Paterson, E. G. and Baker, W. J., "Simulation of Steady Circulation Control for Marine-Vehicle Control Surfaces," AIAA Paper 2004–0748, 2004.

[5]Chang, P. A., Slomski, J. F., Marino, T. A., and Ebert, M. P., "Numerical Simulation of Two- and Three-Dimensional Circulation Control Problems," AIAA Paper 2005–0080, 2005.

[6]Swanson, R. C., Rumsey, C. L., and Anders, S. G., "Progress Towards Computational Method for Circulation Control Airfoils," AIAA Paper 2005–0089, 2005.

[7]Englar, R. J., Smith, J. J., Kelly, S. M., and Rover III, R. C., "Application of Circulation Control to Advanced Subsonic Transport Aircraft, Part I: Airfoil Development," *Journal of Aircraft*, Vol. 31, No. 5, Sept. 1994, pp. 1160–1168.

[8]Lui, Y., Sankar, L. N., Englar, R. J., Ahuja, K. K., and Gaeta, R., "Computational Evaluation of the Steady and Pulsed Jet Effects on the Performance of a Circulation Control Wing Section," AIAA Paper 2004–0056, 2004.

[9]Jones, G. S., Viken, S. A., Washburn, A. E., and Cagle, C. M., "An Active Flow Circulation Controlled Flap Concept for General Aviation Aircraft Applications," AIAA Paper 2002–3157, 2002.

[10]Jones, G. S., Yao, C. S., and Allan, B. G., "Experimental Investigation of a 2D Supercritical Circulation- Control Airfoil Using Particle Image Velocimetry," AIAA Paper 2006–3009, 2006.

[11]Anderson, W. K. and Bonhaus, D. L., "An Implicit Upwind Algorithm for Computing Turbulent Flows on Unstructured Grids," *Computers and Fluids*, Vol. 23, No. 1, 1994, pp. 1–22.

[12]Anderson, W. K., Rausch, R. D., and Bonhaus, D. L., "Implicit/Multigrid Algorithms for Incompressible Turbulent Flows on Unstructured Grids," *Journal of Computational Physics*, Vol. 128, No. 2, 1996, pp. 391–408.

[13]Nielsen, E. J., *Aerodynamic Design Sensitivities on an Unstructured Mesh Using the Navier-Stokes Equations and a Discrete Adjoint Formulation*, Ph.D. thesis, Virginia Polytechnic Institute and State University, Blacksburg, VA, 1998.

[14]Nielsen, E. J., Lu, J., Park, M. A., and Darmofal, D. L., "An Implicit, Exact Dual Adjoint Solution Method Implicit, Exact Dual Adjoint Solution Method for Turbulent Flows on Unstructured Grids," *Computers and Fluids*, Vol. 33, No. 9, 2004, pp. 1131–1155, See also AIAA Paper 2003–0272.

[15]Spalart, P. R. and Allmaras, S. R., "One-Equation Turbulence Model for Aerodynamic Flows," AIAA Paper 92–0429, 1992.

[16]Vatsa, V. N. and Wedan, B. W., "Development of a multigrid code for 3-D Navier-Stokes Equations and Its Application to a Grid-Refinement Study," Vol. 18, No. 18, Jan. 1990, pp. 391–403.

[17]Krist, S. L., Biedron, R. T., and Rumsey, C. L., *CFL3D User's Manual (Version 5.0)*, NASA TM-1998-208444, 1998.

[18]Roe, P. L., "Approximate Riemann Solvers, Parameter Vectors, and Difference Schemes," *Journal of Computational Physics*, Vol. 43, 1981, pp. 357–372.

[19]Menter, F. R., "Two-Equation Eddy-Viscosity Turbulence Models for Engineering Applications," *AIAA Journal*, Vol. 32, No. 8, 1994, pp. 1598–1605.

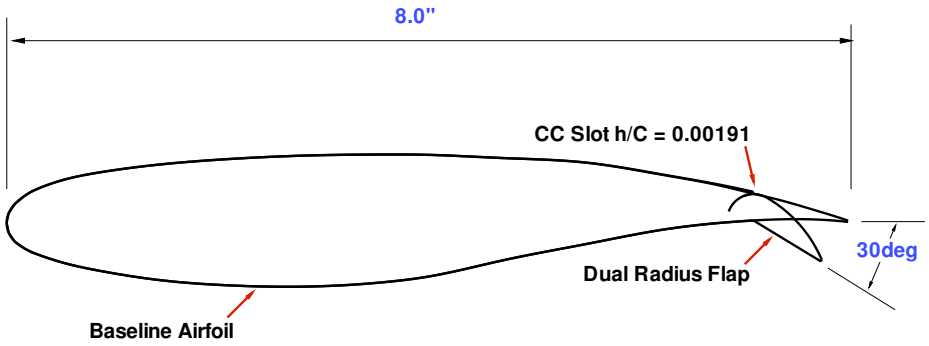

(b) GTRI-DR airfoil profile

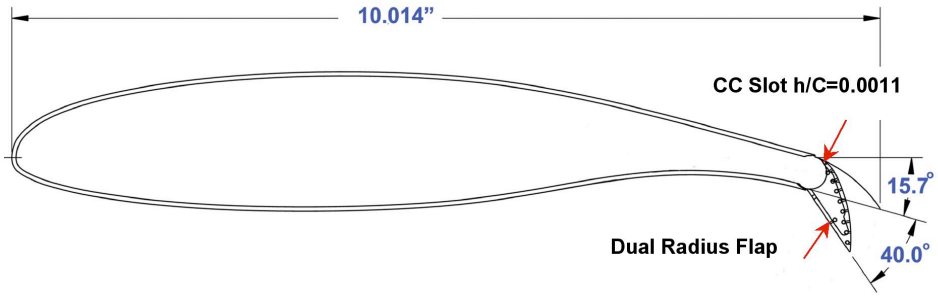

(a) GACC-DR airfoil profile (note that the CC slot height is for the circular trailing edge configuration)

Figure 1. Dual Radius airfoil profiles.

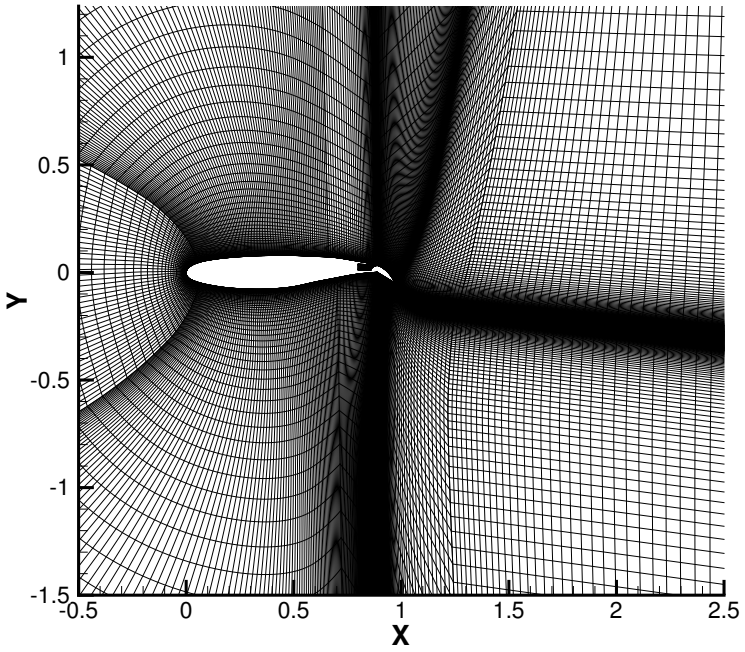

(a) Partial view of grid

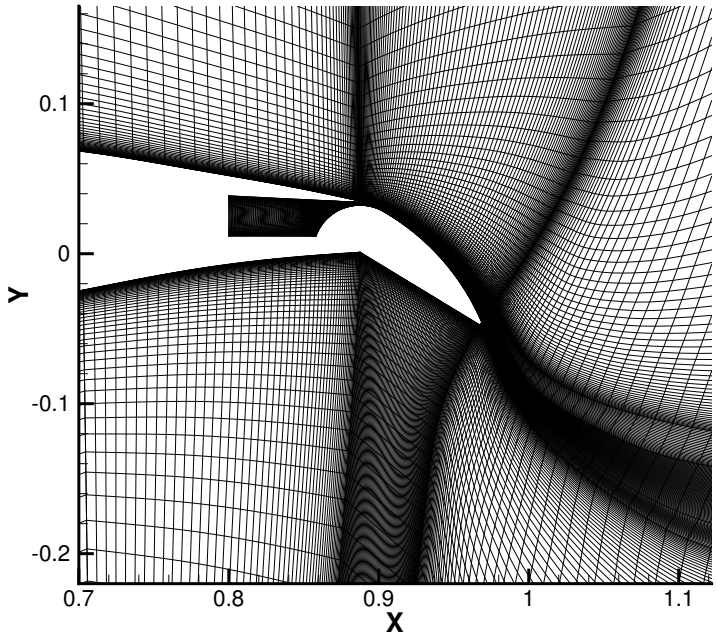

(b) Close up view of grid near jet slot and trailing edge

Figure 2. GTRI-DR airfoil structured grid.

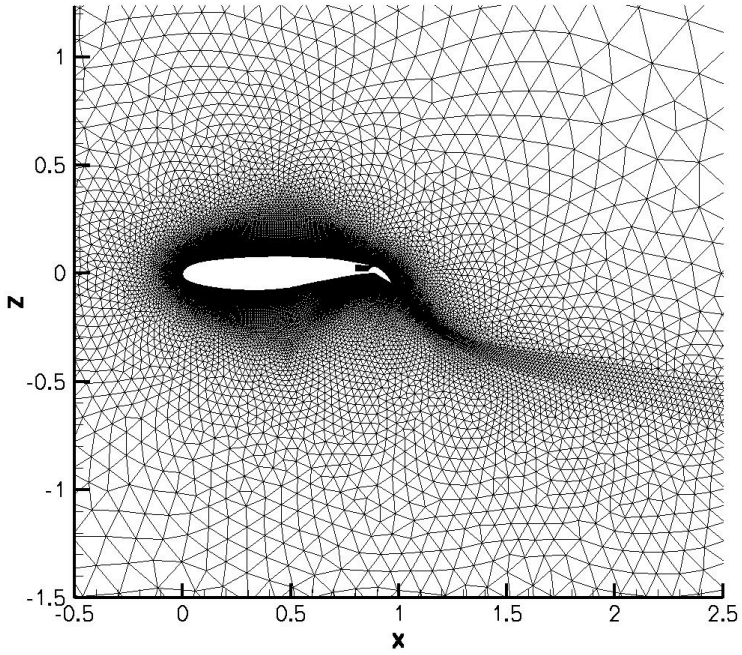

(a) Partial view of grid

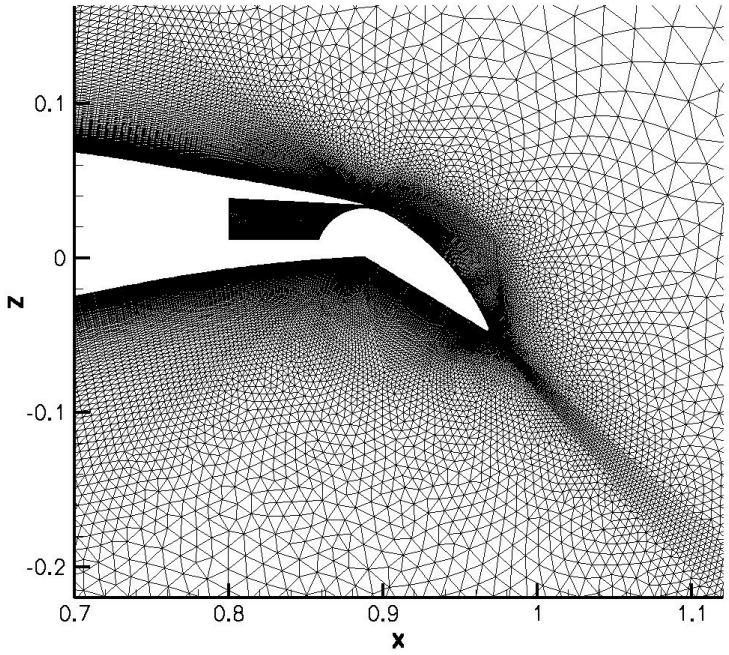

(b) Close up view of grid near jet slot and trailing edge

Figure 3. GTRI-DR unstructured grid.

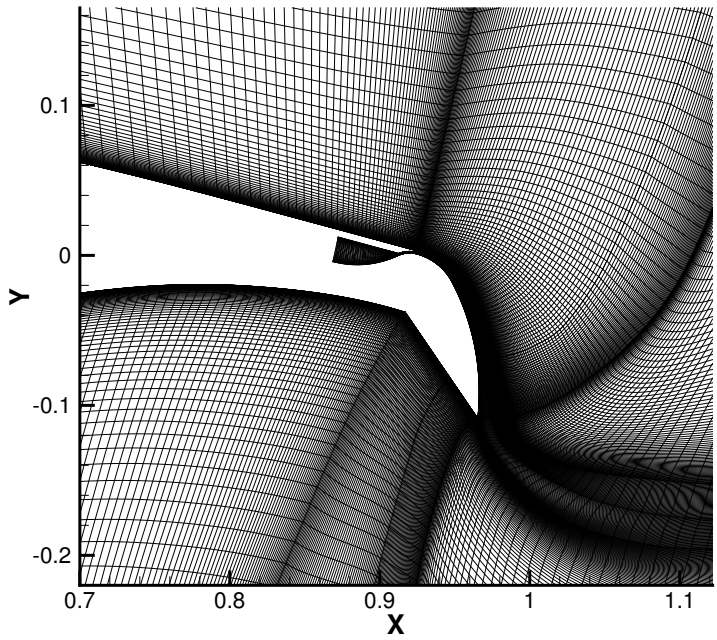

(a) Close up view of the structured grid

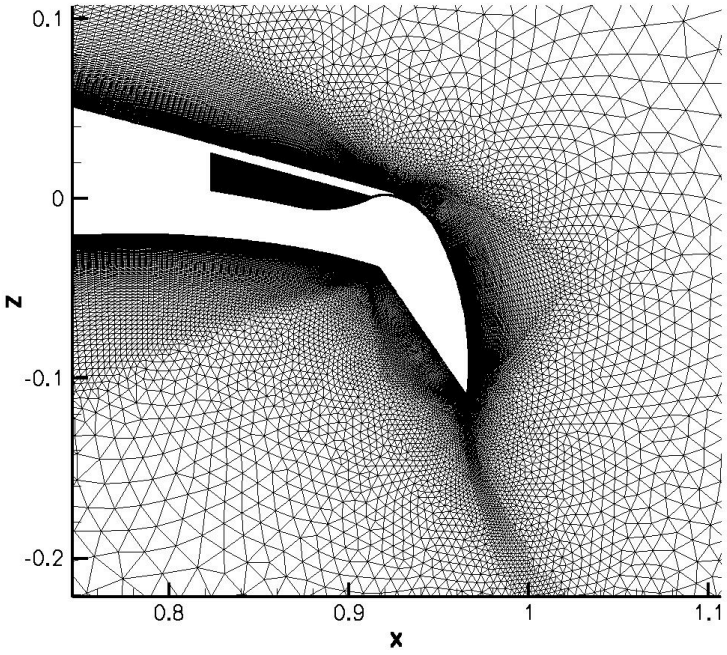

(b) Close up view of the unstructured grid

Figure 4. Structured and Unstructured GACC-DR grids near the jet slot and trailing edge.

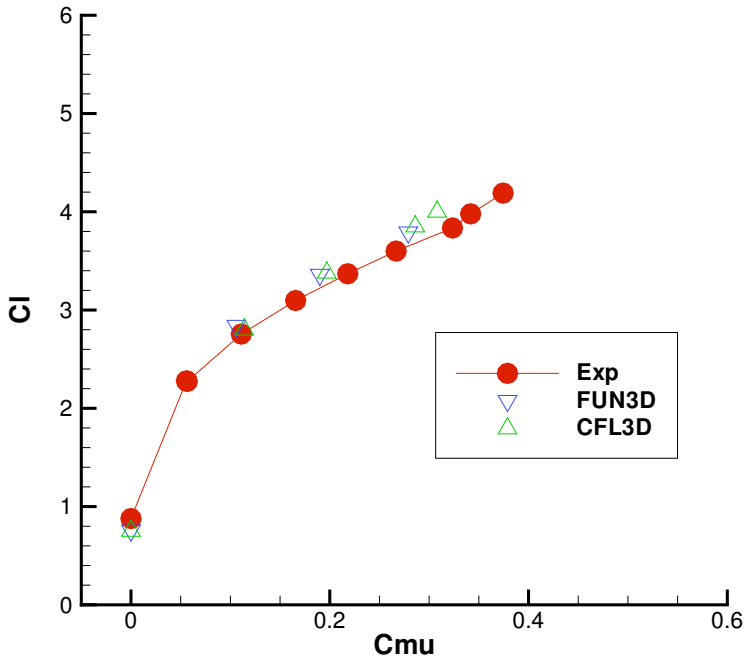

(a) GTRI-DR airfoil at freestream $M_\infty = 0.0842$ and $Re_c = 0.37x10^6$

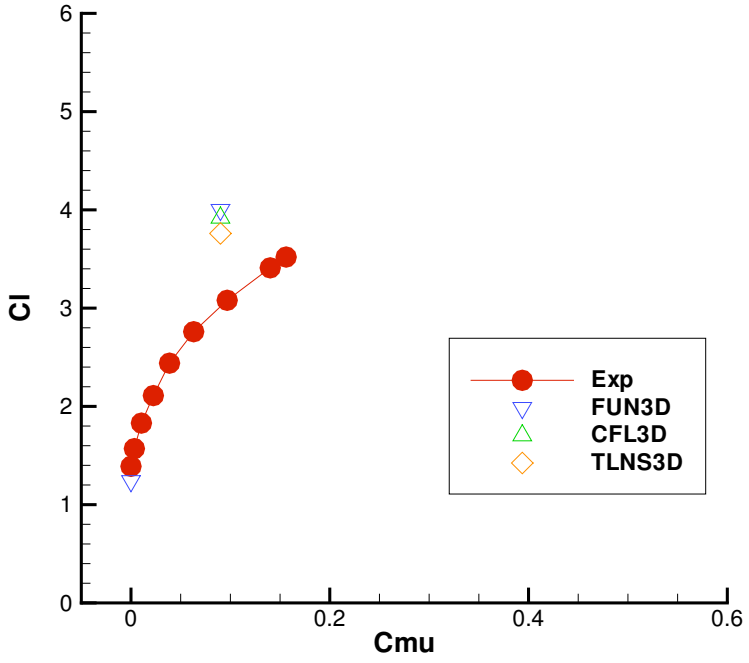

(b) GACC-DR airfoil at freestream $M_\infty = 0.0824$ and $Re_c = 0.47x10^6$

Figure 5. Variation of experimental and computational lift coefficient with blowing coefficient for the dual radius airfoils.

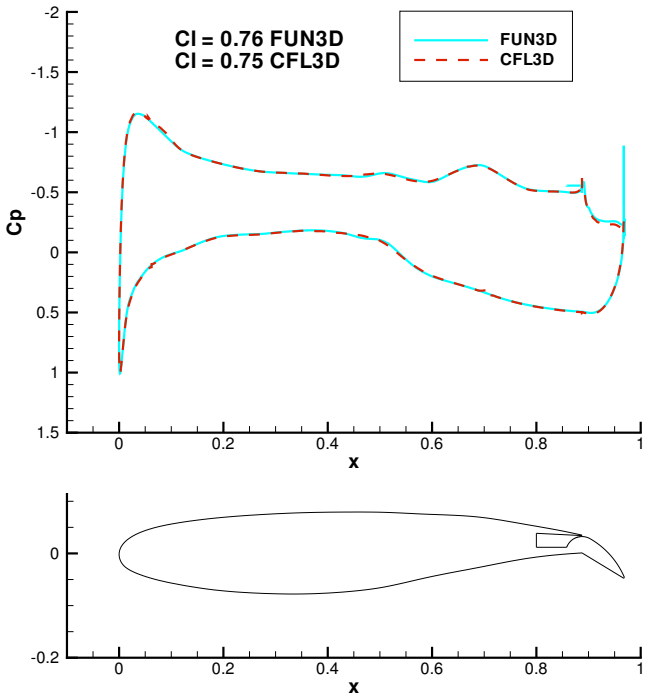

Figure 6. Code to code comparison of GTRI-DR airfoil chordwise pressure distributions at $C_\mu = 0.0$.

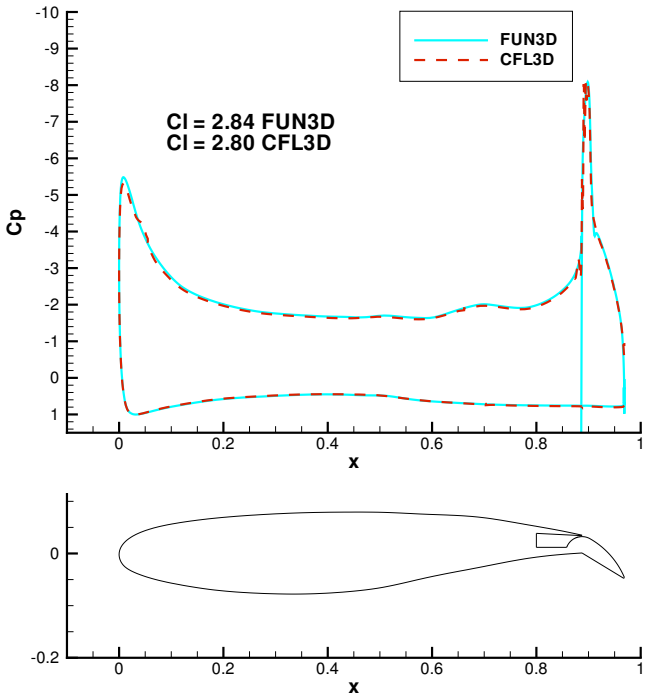

Figure 7. Code to code comparison of GTRI-DR airfoil chordwise pressure distributions at $C_\mu = 0.11$ experimental condition.

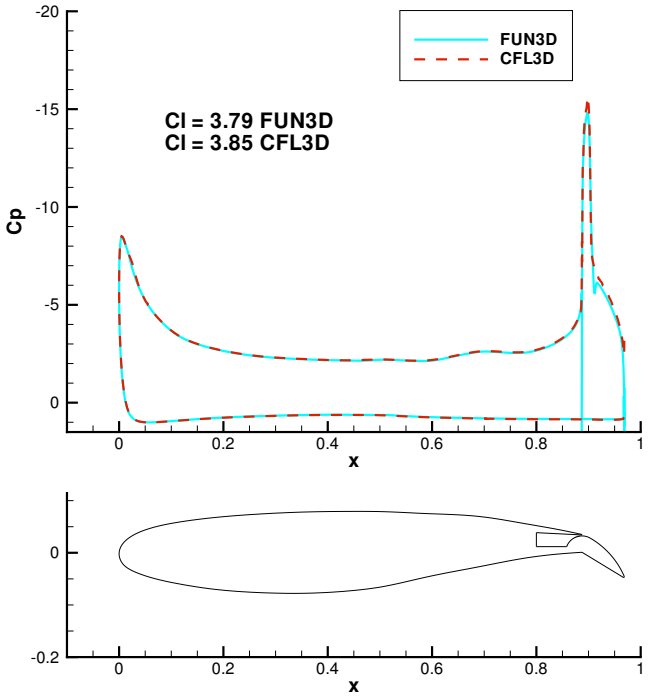

Figure 8. Code to code comparison of GTRI-DR airfoil chordwise pressure distributions at $C_\mu = 0.32$ experimental condition.

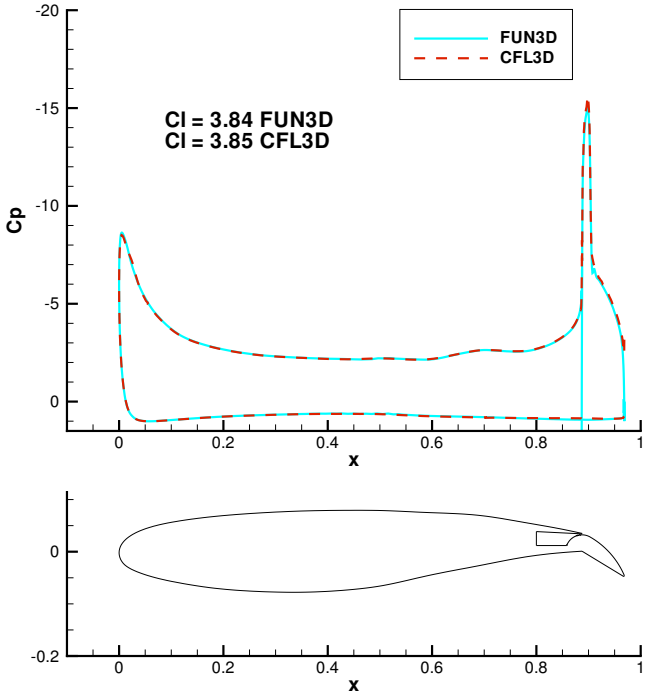

Figure 9. Effect of normal grid refinement on unstructured grid (FUN3D) GTRI-DR airfoil chordwise pressure distribution at $C_\mu = 0.32$ experimental condition.

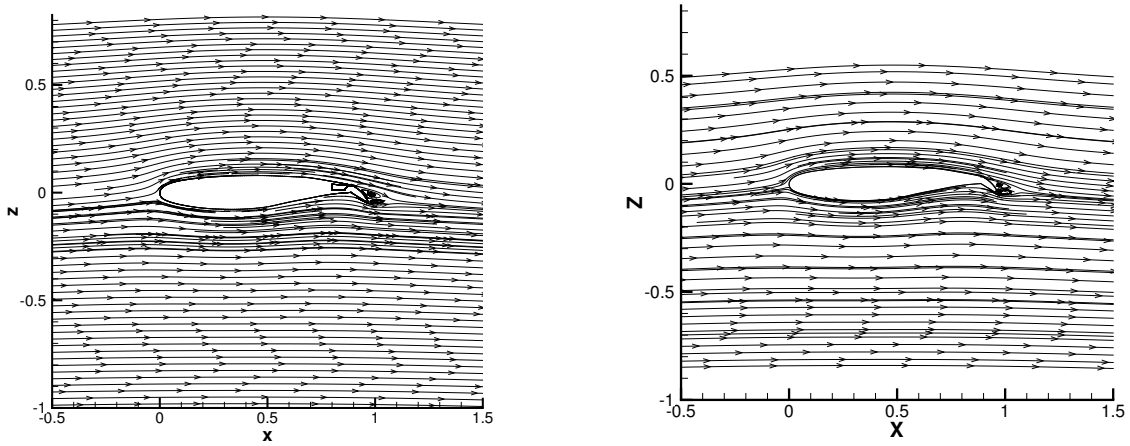

(a) $C_\mu = 0.0$ experimental condition

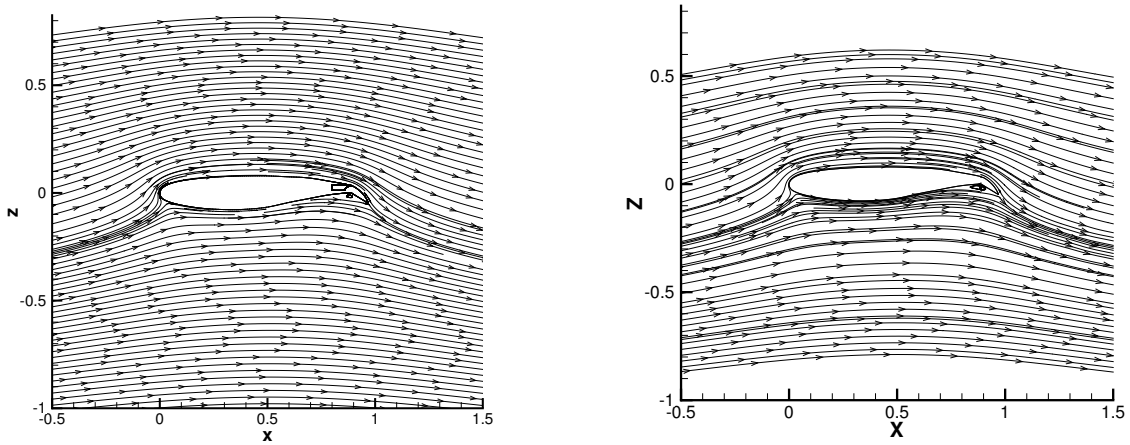

(b) $C_\mu = 0.11$ experimental condition

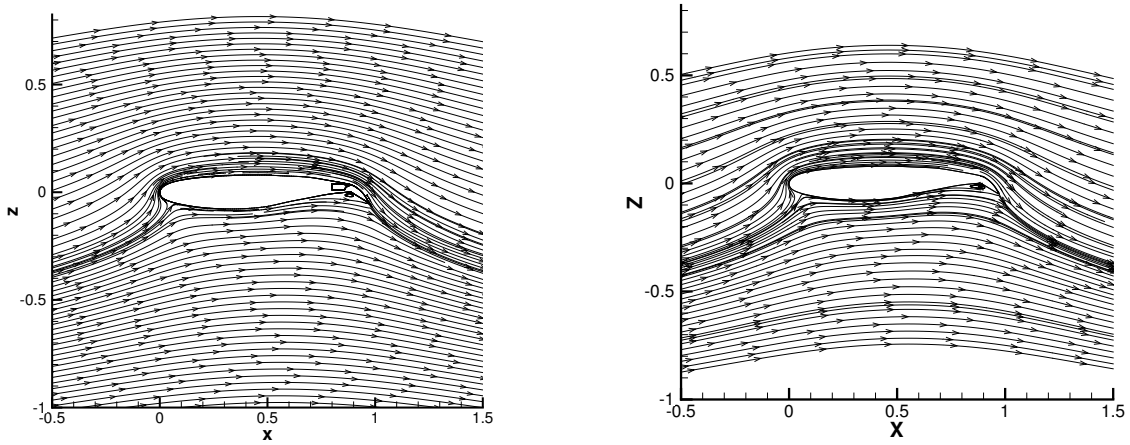

(c) $C_\mu = 0.32$ experimental condition

Figure 10. Comparison of unstructured grid(left) and structured grid(right) GTRI-DR airfoil streamtraces.

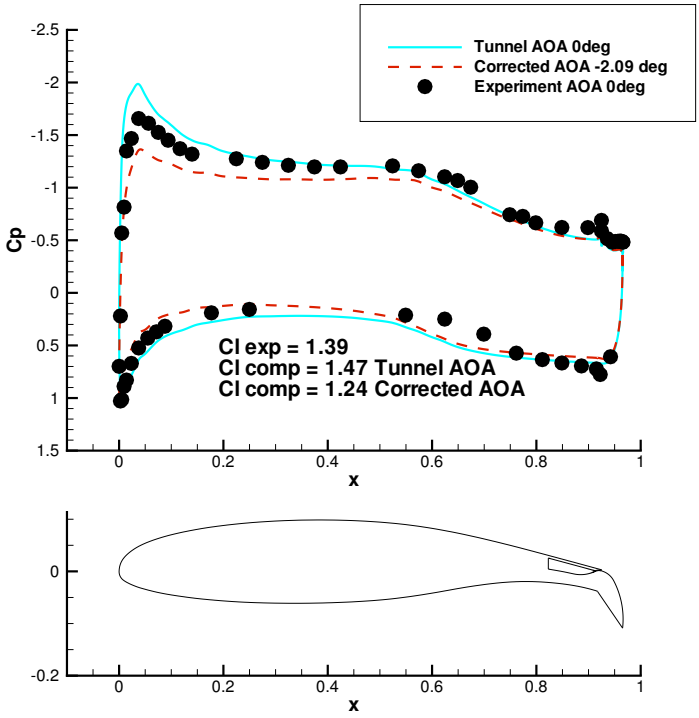

Figure 11. Effect of angle of attack corrections on GACC-DR airfoil FUN3D chordwise pressure distributions at $C_\mu = 0$.

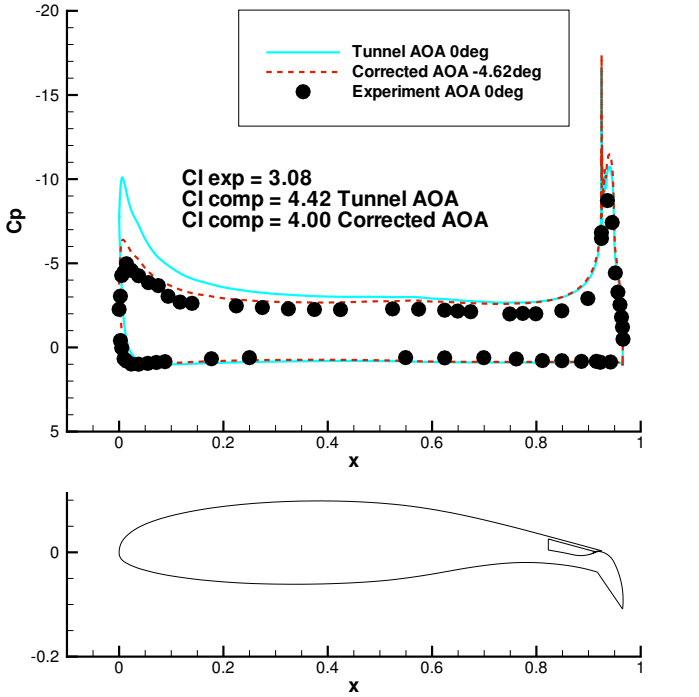

Figure 12. Effect of angle of attack corrections on GACC-DR airfoil FUN3D chordwise pressure distributions at $C_\mu = 0.09$.

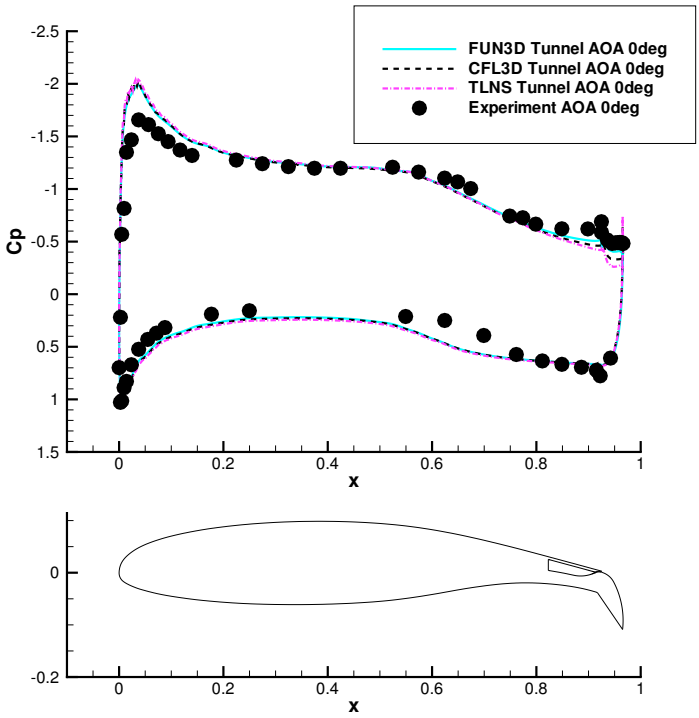

Figure 13. Code to code comparison of GACC-DR airfoil chordwise pressure distributions at $C_\mu = 0$.

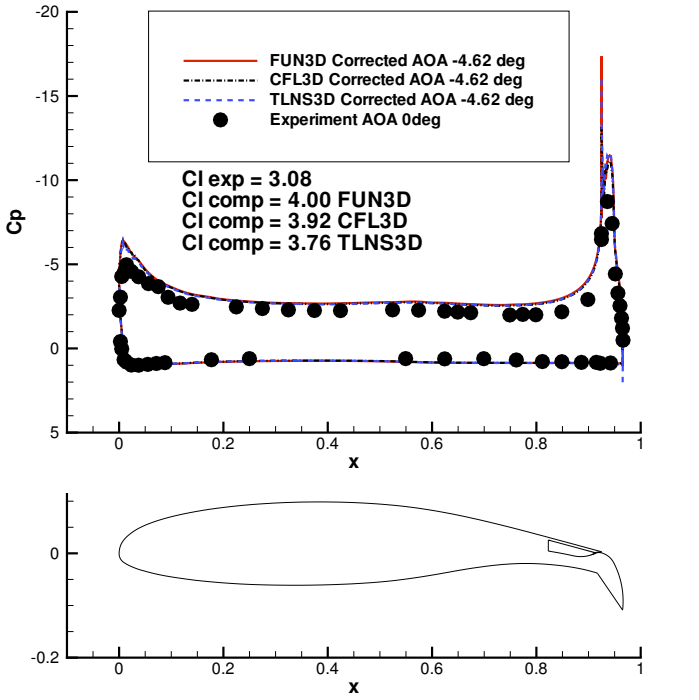

Figure 14. Code to code comparison of GACC-DR airfoil chordwise pressure distributions at $C_\mu = 0.09$.

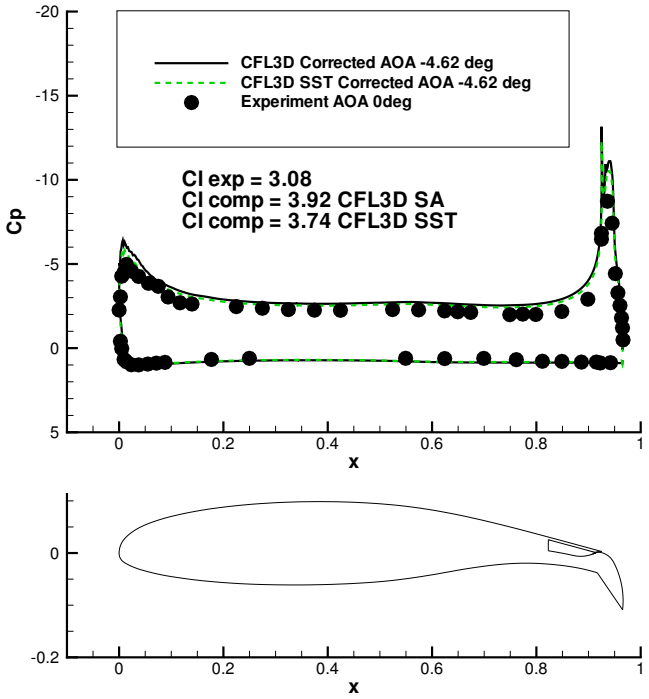

Figure 15. Turbulent model comparison of GACC-DR airfoil chordwise pressure distributions at $C_\mu = 0.09$.

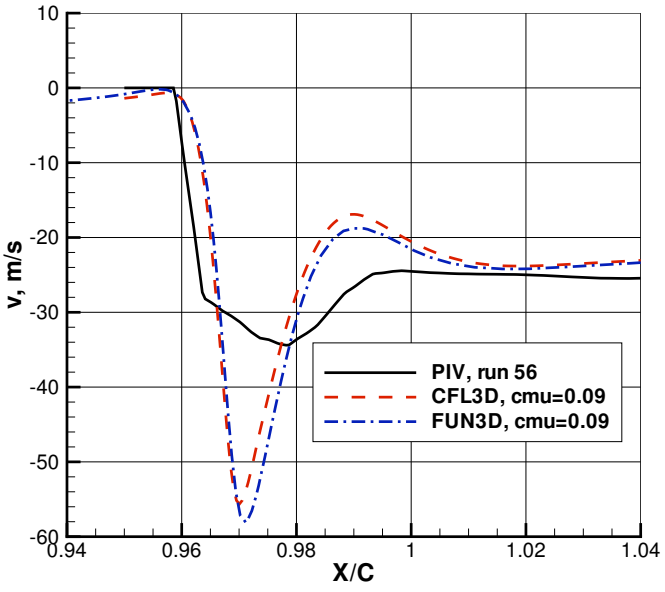

Figure 16. Comparison of experimental and computational vertical velocity behind the trailing edge of the GACC-DR airfoil at $y/c = -0.13$.